Research Article Vol. 42, No. 10 / October 2025 / Journal of the Optical Society of America A 1571

Journal of the Optical Society of America A
OPTICS, IMAGE SCIENCE, AND VISION

Highly sensitive dual eccentric-core D-type PQF-SPR methane sensor

Yudan Sun,[1] Kaiyu Wang,[2] Li Liu,[3] Xinrui Li,[2] Xiaoxu Zhang,[2] Qiang Liu,[2] Wei Liu,[2] Jingwei Lv,[2] Paul K. Chu,[4,5,6] and Chao Liu[2,*]

[1]College of Mechanical and Electrical Engineering, Daqing Normal University, Daqing 163712, China
[2]School of Physics and Electronic Engineering, Northeast Petroleum University, Daqing 163318, China
[3]No. 5 Oil Production Plant of Daqing Oilfield Co., Ltd., Daqing 163513, China
[4]Department of Physics, City University of Hong Kong, Tat Chee Avenue, Kowloon, Hong Kong SAR, China
[5]Department of Materials Science and Engineering, City University of Hong Kong, Tat Chee Avenue, Kowloon, Hong Kong SAR, China
[6]Department of Biomedical Engineering, City University of Hong Kong, Tat Chee Avenue, Kowloon, Hong Kong SAR, China
*msm-liu@126.com

Received 27 May 2025; revised 31 July 2025; accepted 28 August 2025; posted 29 August 2025; published 23 September 2025

A novel, to our knowledge, photonic quasi-crystal fiber surface plasmon resonance methane sensor with high sensitivity is designed and analyzed. The dual eccentric-core D-shaped structure enhances the surface plasmon resonance effect. The groove is fabricated on the D-shaped surface, and then zinc oxide and gold films are sequentially deposited on the surface of the grooved structure. Finally, a methane-sensitive film is deposited. The effects of the structural parameters on the sensing properties are analyzed by finite element analysis. The results show that the optimal sensitivity and average wavelength sensitivity are 140 nm/% and 71.43 nm/% for methane concentrations in the range of 0%–3.5%. Owing to its small size, high sensitivity, and real-time online monitoring capabilities, the sensor has significant commercial potential in methane leakage detection.

https://doi.org/10.1364/JOSAA.569072

1. INTRODUCTION

In the field of energy security and environmental monitoring, methane sensors play a crucial role in these fields; hence, the miniaturization of sensors has become a research hotspot [1–3]. The common gas sensors are catalytic combustion-type methane gas sensors [4], electrochemical methane sensors [5], semiconductor methane sensors [6], absorption spectroscopy-based methane sensors [7], and refractive index-sensitive fiber-optic methane sensors [8]. These methane sensors suffer from various drawbacks. For instance, the catalytic combustion-type sensor requires a specific operating temperature, and the performance is influenced by the other combustible gases. The electrochemical sensor has a relatively short operating life and is sensitive to humidity, while the semiconductor sensor exhibits poor stability, and the optical absorption spectroscopy-based sensor is expensive [9,10]. Hence, researchers have been attempting to develop refractive index-sensitive optical fiber methane sensors. In this type of sensor, the refractive index of the methane-sensitive material varies with methane concentration.

In recent years, optical fiber surface plasmon resonance (SPR) sensing technology has experienced rapid development since it has advantages such as resistance to electromagnetic interference, high sensitivity, good stability, and long-distance transmission capability. Additionally, SPR is very sensitive to the refractive index of the medium being measured, rendering it suitable for methane detection [11,12]. However, the traditional prism SPR refractive index sensors are bulky, consequently limiting the application scope, in addition to the relatively poor sensitivity. In order to miniaturize the structure and improve the sensing properties, SPR sensors based on microstructured fibers have been proposed. Besides the flexible structure, these sensors exhibit enhanced SPR, which enables high-sensitivity detection of methane [13] and has garnered commercial interest [14,15]. Liu *et al*. [16] have designed a photonic crystal fiber (PCF)-based SPR methane sensor with a methane-sensitive film deposited inside the oversized air holes in the cladding, boasting a sensitivity for methane of −1.99 nm/%. However, this sensor requires plasmonic materials and methane-sensitive films to be coated on the inner wall of the air holes, consequently making the fabrication process complex. Liu *et al*. [17] have proposed a PCF-based methane sensor with a dual-core structure with the methane-sensitive film cryptophane-E coated on the groove surface, showing a methane detection sensitivity of 4.60 nm/%. Xiao *et al*. [18] have designed an anchor-shaped PCF-SPR gas sensor composed of a gold film and cryptophane-A as the plasmonic and methane-sensitive materials, respectively. The average methane sensitivity is −4.84 nm/%. To further improve the sensitivity, Xu *et al*. [19] have designed a

dual-core D-shaped PCF. The gold film and methane-sensitive film cryptophane-E are deposited on the open circular surface sequentially, and the methane sensitivity is 11.52 nm/%. These studies reveal that the plasmonic materials play a crucial role in the sensitivity. Liu *et al*. [20] have compared the effects of different coating materials (Au-TiO_2, Au-MgF_2, and Au–ITO) on the sensing performance and proposed a photonic quasi-crystal fiber (PQF) SPR sensor based on a double-layer Au-TiO_2 film. In the methane concentration range of 0%–3.5%, the maximum wavelength sensitivity and average wavelength sensitivity are 40 nm/% and 34.74 nm/%, respectively.

Herein, a dual eccentric-core D-shaped structure PQF-SPR methane sensor is designed. The gold film, zinc oxide film, and methane-sensitive film cryptophane-E are sequentially coated on the polished air holes. The dual-core modes can provide a stronger evanescent field, which effectively enhances the SPR excitation efficiency and generates a more sensitive resonance response. In the methane concentration range of 0%–3.5%, the maximum wavelength sensitivity reaches 140 nm/%. Its sensing performance is significantly better than the aforementioned sensors.

2. STRUCTURE AND ANALYSIS

The cross-sectional structure of the dual eccentric-core D-shaped PQF-SPR sensor is depicted in Fig. 1(a). It is based on the eight-fold PQF structure, as shown in Fig. 1(b). The cladding consists of five layers of air holes, and two air holes are removed from the second layer to form the dual eccentric-core structure. The diameter of the upper two air holes in the third layer is d_3, the diameter of the upper air holes in the fourth layer is d_1, and the diameter of the remaining air holes is d_2. The lattice spacing of the PQF is Λ, and the two upper air holes in the fifth layer are removed. The preformed rod of the designed PQF can be processed by laser drilling. Then the fiber can be fabricated through drawing. The fiber can be polished to form a D-type structure with a polishing depth of h by conventional polishing [21,22]. The top air holes in the fourth layer form the groove structure. Zinc oxide (ZnO) and gold (Au) films with thicknesses of t_{ZnO} and t_{Au} are deposited sequentially on the groove by magnetron sputtering [23] or chemical vapor deposition (CVD) [24]. Finally, the methane-sensitive film cryptophane-E with a thickness of t_{CH4} is deposited. The initial parameters of the structure are as follows: $\Lambda = 3$ μm, $d_1 = 2.6$ μm, $d_2 = 2$ μm, $d_3 = 1.2$ μm, $d_c = 3.5$ μm, $t_{CH4} = 500$ nm, $t_{Au} = 27$ nm, $t_{ZnO} = 10$ nm, and $h = 6.8$ μm. The radius of the PQF is $R = 9$ μm, and the outermost layer is a perfect match layer. The PQF is made of silica, and its refractive index variation with wavelength can be calculated using the Sellmeier dispersion relation [25]:

$$n_{\text{Silica}}^2 - 1 = \frac{A_1\lambda^2}{\lambda^2 - B_1^2} + \frac{A_2\lambda^2}{\lambda^2 - B_2^2} + \frac{A_3\lambda^2}{\lambda^2 - B_3^2}, \tag{1}$$

where λ represents the operating wavelength with the unit in μm. $A_1 = 0.6961663$, $A_2 = 0.4079426$, $A_3 = 0.8974794$, $B_1 = 0.0684043$, $B_2 = 0.1162424$, and $B_3 = 9.896161$.

The dielectric constant of gold is given by the Drude–Lorentz model [26]:

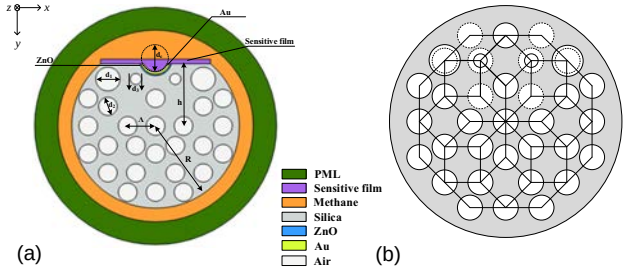

Fig. 1. (a) Cross-section of the PQF-SPR sensor and (b) eight-fold Penrose PQF structure.

$$\varepsilon_{\text{Au}} = \varepsilon_\infty - \frac{\omega_D^2}{\omega(\omega + i\gamma_D)} - \frac{\Delta\varepsilon \cdot \Omega_L^2}{(\omega^2 - \Omega_L^2) + i\Gamma_L\omega}, \tag{2}$$

where $\varepsilon_\infty = 5.9673$ represents the high-frequency dielectric constant of gold, $\Delta\varepsilon = 1.09$ is the weighting factor, and $\omega_D/2\pi$ and $\gamma_D/2\pi$ represent the plasma frequency and damping frequency with values of 2113.6 and 15.92 THz, respectively. $\Gamma_L/2\pi = 104.86$ and $\Omega_L/2\pi = 650.07$ THz are the spectral width and spectral frequency of the Lorentz oscillator, respectively.

Zinc oxide (ZnO) is a semiconductor material with a wider bandgap and high electron mobility, which is higher than that of other similar materials [27]. The higher electron mobility is conducive to the rapid response of the optical fiber sensors. Meanwhile, it has excellent electrical properties and chemical stability [28], and the Au–ZnO composite films can enhance the sensing performance of the sensor. The dielectric constant of ZnO can be derived using the Drude model [29]:

$$\varepsilon(\omega) = \varepsilon_\infty - \frac{\omega_p^2}{\omega^2 + \gamma^2} + \mathrm{i}\frac{\gamma \cdot \omega_p^2}{\omega(\omega^2 + \gamma^2)}, \tag{3}$$

where $\varepsilon_\infty = 3.40$ is the high-frequency dielectric constant, $\omega_p = 2 \times 10^{15}$ Hz is the plasma frequency, and $\gamma = 1.5 \times 10^{14}$ Hz is the damping frequency. Cryptophane-E is a cage-like molecule. When methane molecules enter the cage-like structure, the dipole moment is altered, resulting in refractive index variations in the sensitive film. In the methane concentration range between 0% and 3.5%, the refractive index n of the sensitive film changes linearly with the methane concentration C_CH_4, as shown by the following relationship [30]:

$$n = 1.448 - 0.0046\text{C\_CH}_4. \tag{4}$$

When the methane concentration changes, the refractive index variation is manifested as a shift in the loss spectrum of the PQF-SPR sensor. By analyzing the relationship between the peak wavelength of the loss spectrum and methane concentration, the methane concentration can be determined [31]. The relationship of the loss spectrum of the PQF-SPR sensor is [32]

$$\text{CL}\left(\frac{\text{dB}}{\text{cm}}\right) = 8.686 \times \frac{2\pi}{\lambda} \times \text{Im}(n_{\text{eff}}) \times 10^4, \tag{5}$$

where $k_0 = 2\pi/\lambda$ is the wave number, and $\text{Im}(n_{\text{eff}})$ is the imaginary part of the effective refractive index. To evaluate the performance of the sensor, the wavelength sensitivity of the methane sensor is typically defined as [33]

$$S_\lambda\left(\frac{\text{nm}}{\%}\right)=\frac{\Delta\lambda}{\Delta \text{C\_CH}_4}, \tag{6}$$

where ΔC_CH_4 represents the change of the methane concentration, and $\Delta\lambda$ is the wavelength shift corresponding to the peak value of the loss spectrum.

3. RESULTS AND DISCUSSION

Figure 2 shows the loss spectrum of the sensor for a methane concentration of 0.5% and the dispersion relations of the core mode and surface plasmon polariton (SPP) mode. The red solid line and red dashed-dotted line represent the real part of the effective refractive index of the y-polarized core mode and SPP mode, respectively. These two curves intersect at 950 nm, where the phase-matching condition is satisfied, and the core mode excites the SPP mode. Figure 2(a) exhibits the electric-field distribution of the y-polarized core mode. The two core modes are coupled to Au–ZnO on the groove surface through the gap of the air holes. The electric field is enhanced on the groove surface, which is close to the fiber core. Hence, the dual-core structure improves the coupling strength between the core mode and SPP mode. Meanwhile, the SPP mode is also partially coupled back to the fiber core, as shown in Fig. 2(b). As a result, the transmission loss of the y-polarized core mode reaches the maximum, which corresponds to the peak in the loss spectrum indicated by the black solid line. Similarly, the loss spectrum of the x-polarized core mode is calculated and shown by the black dashed-dotted line in Fig. 2(b). Compared with the loss spectrum of the y-polarized core mode, the loss spectrum of the x-polarized mode is negligible. Therefore, the wavelength shift corresponding to the peak of the loss spectrum of the y-polarized core mode is used to evaluate the performance of the methane sensor.

The properties of the PQF-SPR methane sensor are influenced by the plasmonic material and the structure of the PQF. To achieve the optimal methane-sensing characteristics, the structural parameters of the sensor are optimized systematically. The wavelength sensitivity of the y-polarized core mode is used as the evaluation index. The effect of the gold film thickness t_{Au} on the sensitivity is first analyzed. The loss spectra for different

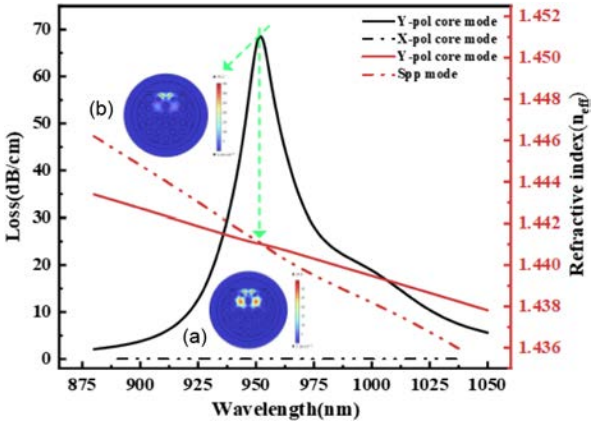

Fig. 2. Loss spectrum of the PQF-SPR sensor and dispersion relationship of the core mode and SPP mode with (a) showing the electric field diagram of the y-polarized core mode and (b) electric-field diagram of the SPP mode.

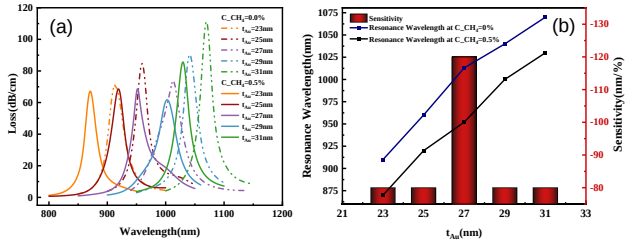

Fig. 3. (a) Loss spectra and (b) resonance wavelengths and sensitivities for different values of t_{Au}.

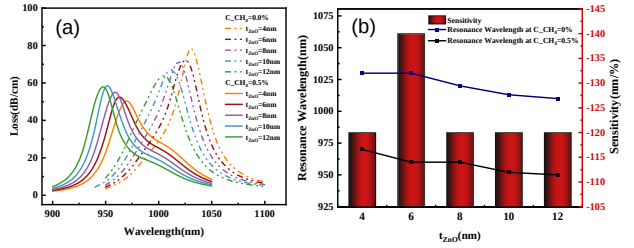

Fig. 4. (a) Loss spectra and (b) resonance wavelengths and sensitivities for different values of t_{ZnO}.

gold film thicknesses for methane concentrations of 0% and 0.5% are shown in Fig. 3(a). As the gold film thickness t_{Au} is changed from 23 to 31 nm, the loss spectrum shifts toward longer wavelengths because the effective refractive index of the core mode is only affected by the structural parameters of PQF, which are almost constant. In contrast, the effective refractive index of the SPP mode increases with the gold film thickness, causing the intersection point (phase-matching point) of the core mode and SPP mode dispersion curves to shift. Therefore, the resonance wavelength redshifts. Figure 3(b) shows the resonance wavelength and wavelength sensitivity for different gold film thickness. The wavelength sensitivity increases and then decreases with increasing gold film thicknesses. When $t_{Au}=27$ nm, the resonance wavelength shifts from 1010 nm for C_$CH_4=0\%$ to 950 nm for C_$CH_4=0.5\%$, achieving the maximum wavelength sensitivity of 120 nm/%. Therefore, $t_{Au}=27$ nm is selected.

Similarly, the thickness of the zinc oxide (ZnO) film is optimized. When t_{ZnO} is varied between 4 and 12 nm, the effects of different ZnO film thicknesses on the loss spectrum are shown in Fig. 4(a). A larger t_{ZnO} causes the phase-matching point of the y-polarized core mode and the SPP mode to shift toward a shorter wavelength, showing a blueshift in the loss spectrum. Figure 4(b) shows the impact of different ZnO film thicknesses on the wavelength sensitivity of the sensor. When $t_{ZnO}=6$ nm, the resonance wavelength shifts from 1030 nm for 0% methane concentration to 960 nm for 0.5% methane concentration, exhibiting the optimal wavelength sensitivity of 140 nm/%.

Figure 5(a) shows the effects of different polishing depths h on the loss spectrum. The loss spectrum shifts toward longer wavelengths as h is increased from 6.6 to 7.0 μm. This is because the effective refractive index of the core mode decreases with increasing polishing depth h, thereby producing a redshift of the phase matching point. At the same time, a larger h causes the plasmonic medium on the D-shaped surface to be closer to the

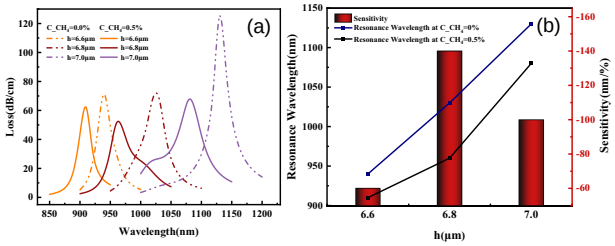

Fig. 5. (a) Loss spectra and (b) resonance wavelengths and sensitivities for different values of h.

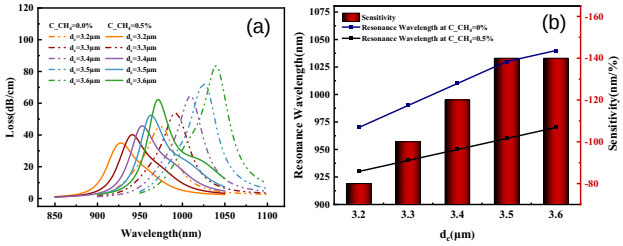

Fig. 6. (a) Loss spectra and (b) resonance wavelengths and sensitivities for different values of d_c.

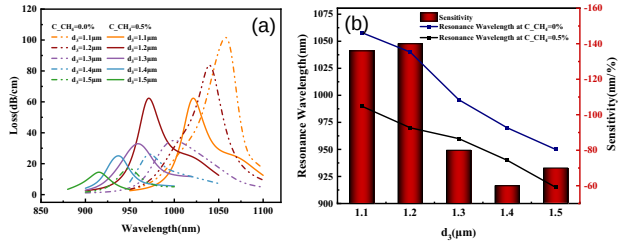

Fig. 7. (a) Loss spectra and (b) resonance wavelengths and sensitivities for different values of d_3.

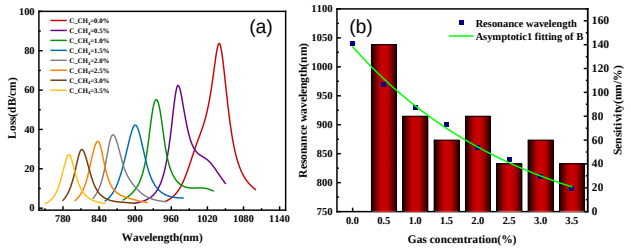

Fig. 8. (a) Loss spectra for different methane concentrations and (b) resonance wavelengths and fitted curve.

two fiber cores to enhance the coupling between the y-polarized core mode and the SPP mode, resulting in an increase in the loss peak. Figure 5(b) presents the resonance wavelength and wavelength sensitivities for different polishing depths h. When the methane concentration is increased from 0% to 0.5%, the sensitivities for $h = 6.6$ μm, $h = 6.8$ μm, and $h = 7.0$ μm are 60 nm/%, 140 nm/%, and 100 nm/%, respectively. Therefore, $h = 6.8$ μm is selected as the optimal value.

The size of the groove, which directly affects the position of the plasmonic materials, corresponds to the original pore size d_c . Figure 6(a) shows the loss spectra for different diameters d_c when the methane concentration is changed from 0% to 0.5%. As d_c goes up from 3.2 to 3.6 μm, the loss spectrum shifts toward longer wavelengths, and the loss peak increases with increasing d_c. This is mainly because a larger d_c expands the coating area of the surface plasmonic materials and reduces the distance between the SPP mode and the y-polarized core mode, thereby enhancing the surface plasmon resonance effect. Figure 6(b) presents the resonance wavelength and wavelength sensitivities for different d_c. When $d_c = 3.6$ μm, the sensor shows the highest sensitivity with the largest loss peak and narrowest full-width at half-maximum (FWHM). Therefore, $d_c = 3.6$ μm is selected as the optimal parameter.

The air holes in the PQF play a key role in confining the fiber core mode, and their size directly affects the coupling between the core mode and the SPP mode as well as the effective refractive index of the core mode. In particular, the upper two air holes with a diameter of d_3 and the plasmonic materials affect the sensing properties. Figure 7(a) shows that the loss spectrum shifts toward a shorter wavelength as d_3 is increased from 1.1 to 1.5 μm, and the loss peak gradually decreases. This is because a bigger d_3 narrows the coupling channel between the core mode and the SPP mode. The fiber core mode is better confined in the fiber core, and the energy coupling between the core mode and the SPP mode weakens, resulting in a decrease in the loss peak. When the methane concentration is increased from 0% to 0.5%, the wavelength sensitivities for different d_3 values are shown in Fig. 7(b). The wavelength sensitivities increase initially and then decrease with increasing d_3. The maximum sensitivity is observed for $d_3 = 1.2$ μm.

According to the above analysis and optimization, the optimal structural parameters of the sensor are determined as follows: $\Lambda = 3$ μm, $d_1 = 2.6$ μm, $d_2 = 2$ μm, $d_3 = 1.2$ μm, $d_c = 3.6$ μm, $t_{CH4} = 500$ nm, $t_{Au} = 27$ nm, $t_{ZnO} = 6$ nm, and $h = 6.8$ μm. As the methane concentration is varied from 0% to 3.5% with a step size of 0.5%, the loss spectra are shown in Fig. 8(a). With increasing methane concentration, the loss spectra shift toward shorter wavelengths, and the loss peaks decrease continuously. This is because the decrease in the resonance wavelength reduces the imaginary part of the refractive index of gold and absorption loss. Figure 8(b) shows the variation of the resonance wavelengths with increasing methane concentration. The resonance wavelength of the loss spectrum blueshifts due to the decrease in the refractive index of the methane-sensitive film as the methane concentration is increased. The effective refractive index of the SPP mode decreases, while the effective refractive index of the core mode does not change. A curve with a fitting degree of 99.6% can be established to fit the relationship between the resonance wavelength and methane concentration. It means that the methane concentration can be measured continuously in the range of 0%–3.5% with maximum and average sensitivities of 140 nm/% and 71.43 nm/%, respectively.

Table 1 compares the properties of methane sensors reported recently. It is evident that the PQF-SPR methane sensor described in this paper has better wavelength sensitivity due to the dual eccentric-core D-shaped structure. The maximum wavelength sensitivity and average wavelength sensitivity are also superior, indicating strong potential for high-sensitivity

Table 1. Comparison of the Properties of Our Sensor with Those of Recently Reported Sensors

References	Sensing Methodology	Concentration Range (%)	Max. Wave Sensitivity (nm/%)	Average Wave Sensitivity (nm/%)
Ref. [16]	Internal (PCF)	0%–3.5%	−1.99	N/A
Ref. [17]	External (PCF)	0%–3.0%	4.60	N/A
Ref. [18]	External (PCF)	0.5%–3.0%	−4.84	N/A
Ref. [19]	External (PCF)	0%–3.5%	11.52	N/A
Ref. [34]	External(PCF)	0%–3.5%	6.39	6.643
Ref. [20]	External (PQF)	0%–3.5%	40	34.73
This work	External (PQF)	0%–3.5%	140	71.43

methane detection in environmental monitoring, climate research, industrial safety, and environmental protection.

4. CONCLUSION

A highly sensitive dual eccentric-core D-shaped PQF-SPR methane sensor is designed and analyzed. The sensor utilizes a special air hole arrangement to create the dual eccentric-core effect and employs an Au–ZnO composite film to improve SPR. The methane-sensitive substance cryptophane-E is coated on the surface of the plasmonic material to enable methane concentration detection. Finite element analysis is performed to determine the effects of the structural parameters on the sensing characteristics and to optimize the structure. The optimized sensor delivers excellent methane-sensing performance. In the methane concentration range of 0%–3.5%, the maximum wavelength sensitivity and average wavelength sensitivity are 140 nm/% and 71.43 nm/%, respectively. The results reveal a new approach for the design of high-sensitivity methane sensors, and the sensor has great application potential in methane gas detection.

Funding. Basic Research Support Project for the Excellent Youth Scholars of Heilongjiang Province (YQJH2023077); Hainan Province Science and Technology Special Fund (ZDYF2022GXJS222); Natural Science Foundation of Heilongjiang Province (JQ2023F001, LH2021F007, LH2022F004); China Postdoctoral Science Foundation (2020M670881); City University of Hong Kong Donation Research Grants (DON-RMG 9229021, 9220061).

Disclosures. The authors declare no conflicts of interest.

Data availability. Data underlying the results presented in this paper are not publicly available at this time but may be obtained from the authors upon reasonable request.

REFERENCES

1. T. He, W. Wang, B. G. He, *et al.*, "Review on optical fiber sensors for hazardous-gas monitoring in mines and tunnels," IEEE Trans. Instrum. Meas. **72**, 7003722 (2023).
2. T. Zhang, Y. Zhang, Y. Chang, *et al.*, "Methodology of methane emission accounting in petrochemical and chemical industries of China," IOP Conf. Ser. Earth. Environ. Sci. **398**, 012011 (2019).
3. D. B. Papkovsky and R. I. Dmitriev, "Biological detection by optical oxygen sensing," Chem. Soc. Rev. **42**, 8700–8732 (2013).
4. G. Ulrich, S. Pavel, and M. Chad, "Methane gas sensing technologies in combustion: comprehensive review," J. Electrochem. Sci. Eng. **10**, 103–110 (2020).
5. D. Manan, L. Irene, Z. Y. Chen, *et al.*, "Ultrasensitive electrochemical methane sensors based on solid polymer electrolyte-infused laser-induced graphene," ACS Appl. Mater. Interfaces **11**, 6166–6173 (2019).
6. F. Leonardo, F. Manuel, F. Laercio, *et al.*, "A portable device for methane measurement using a low-cost semiconductor sensor: development, calibration and environmental applications," Sensors **21**, 602 (2021).
7. H. Yang, X. Bu, Y. Cao, *et al.*, "A methane telemetry sensor based on near-infrared laser absorption spectroscopy," Infrared Phys. Technol. **114**, 103670 (2021).
8. Y. Li, H. Chen, H. Li, *et al.*, "Highly sensitive methane gas sensor based on Au/UVCFS films coated D-shaped photonic crystal fiber," Phys. Scr. **98**, 065533 (2023).
9. Y. H. Ahmad, A. T. Mohamed, and S. Y. Al-qaradawi, "Exploring halloysite nanotubes as catalyst support for methane combustion: influence of support pretreatment," Appl. Clay Sci. **201**, 105956 (2021).
10. T. Aldhafeeri, M. Tran, R. Vrolyk, *et al.*, "A review of methane gas detection sensors: recent developments and future perspectives," Inventions **5**, 28 (2020).
11. Z. Wang, P. Gao, S. Liu, *et al.*, "A reflective methane concentration sensor based on biconvex cone photonic crystal fiber," Optik **241**, 166983 (2021).
12. S. Kumar, G. C. Yadav, G. Sharma, *et al.*, "Study of surface plasmon resonance sensors based on silver–gold nanostructure alloy film coated tapered optical fibers," Appl. Phys. A **124**, 695 (2018).
13. B. Hossain, S. Hossain, S. M. R. Islam, *et al.*, "Numerical development of high performance quasi D-shape PCF-SPR biosensor: an external sensing approach employing gold," Results Phys. **18**, 103281 (2020).
14. H. Wang, W. Zhang, C. Chen, *et al.*, "A new methane sensor based on compound film-coated photonic crystal fiber and Sagnac interferometer with higher sensitivity," Results Phys. **15**, 102817 (2019).
15. H. Liu, B. Wu, X. Zhang, *et al.*, "A highly sensitive sensor of methane and hydrogen in tellurite photonic crystal fiber based on four-wave mixing," Opt. Quantum Electron. **54**, 215 (2020).
16. H. Liu, M. Wang, Q. Wang, *et al.*, "Simultaneous measurement of hydrogen and methane based on PCF-SPR structure with compound film-coated side-holes," Opt. Fiber Technol. **45**, 1–7 (2018).
17. H. Liu, H. Wang, C. Chen, *et al.*, "High sensitive methane sensor based on twin-core photonic crystal fiber with compound film-coated side-holes," Opt. Quantum Electron. **52**, 81 (2020).
18. Y. Xiao, Z. Jiang, B. Yin, *et al.*, "Simultaneous measurement of hydrogen and methane concentrations with temperature self-calibration based on a SPR sensor with an anchor-shaped photonic crystal fiber," Opt. Laser Technol. **175**, 110880 (2024).
19. H. Xu, Y. Feng, X. Gan, *et al.*, "A highly sensitive dual-core d-shape photonic crystal fiber based on surface plasmon resonance for methane sensing," Plasmonics **20**, 1341–1349 (2024).
20. Q. Liu, K. Wang, Y. Sun, *et al.*, "Surface plasmon resonance methane sensor based on the D-type photonic quasi-crystal fiber with double-layer films," Opt. Fiber Technol. **84**, 103779 (2024).
21. M. R. Islam, A. N. M. Iftekher, M. F. Etu, *et al.*, "Dual peak double resonance sensing using a dual plasmonic material PCF-SPR sensor," Plasmonics **18**, 983–993 (2023).
22. Q. Xie, Y. Chen, X. Li, *et al.*, "Characteristics of D-shaped photonic crystal fiber surface plasmon resonance sensors with different side-polished lengths," Appl. Opt. **56**, 1550–1555 (2017).
23. M. A. Mahfuz, A. Mollah, M. R. Momota, *et al.*, "Highly sensitive photonic crystal fiber plasmonic biosensor: design and analysis," Opt. Mater. **90**, 315–321 (2019).

24. A. K. Shakya and S. K. Singh, "Design of dual-polarized tetra core PCF based plasmonic RI sensor for visible-IR spectrum," Opt. Commun. **478**, 126372 (2021).
25. Z. Zhang, S. Li, Z. Yin, *et al.*, "Dual-core photonic crystal fiber surface plasmon resonance sensor with high sensitivity and narrow FWHM," Plasmonics **19**, 495–504 (2024).
26. N. Islam, F. H. Arif, M. A. Yousuf, *et al.*, "Highly sensitive open channel based PCF-SPR sensor for analyte refractive index sensing," Results Phys. **46**, 106266 (2023).
27. A. K. Shakya and S. Singh, "Gold-ZnO coated surface plasmon resonance refractive index sensor based on photonic crystal fiber with tetra core in hexagonal lattice of elliptical air Holes," in *Robotics, Control and Computer Vision*, Vol. **1009** of Lecture Notes in Electrical Engineering (2023), pp. 567–576.
28. Y. Wang, X. Meng, and J. Cao, "Rapid detection of low concentration CO using Pt-loaded ZnO nanosheets," J. Hazard. Mater. **381**, 120944 (2020).
29. E. Sachet, J. Maria, M. D. Losego, *et al.*, "Mid-infrared surface plasmon resonance in zinc oxide semiconductor thin films," Appl. Phys. Lett. **102**, 051111 (2013).
30. Q. Liu, J. Zhao, Y. Sun, *et al.*, "High-sensitivity methane sensor composed of photonic quasi-crystal fiber based on surface plasmon resonance," J. Opt. Soc. Am. A **38**, 1438–1442 (2021).
31. F. Wei, X. Zhang, and S. Tang, "Methane gas sensor based on surface plasmon resonance and photonic crystal fiber," Univ. Jinan Sci. Technol. **34**, 636–640 (2020).
32. Z. Zhang, T. Shen, H. Wu, *et al.*, "A temperature sensor based on D-shape photonic crystal fiber coated with Au–TiO_2 and Ag–TiO_2," Opt. Quant. Electron. **53**, 678 (2021).
33. Y. Li, H. Chen, H. Li, *et al.*, "Ultra-high sensitivity methane gas sensor based on Vernier effect in double D-shaped and cryptophane-A film-coated photonic crystal fiber: design and FEM simulation," Results Phys. **52**, 106840 (2023).
34. H. Jiang, T. Shen, Y. Feng, *et al.*, "Characterization of incompletely coated D-shaped PCF-SPR refractive index sensors," Phys. Scr. **98**, 105520 (2023).